Biomedical Optics EXPRESS

Characterization of multiphoton microscopy in the bone marrow following intravital laser osteotomy

Raphaël Turcotte,[1,2] Clemens Alt,[1] Luke J. Mortensen,[1] and Charles P. Lin[1,*]

[1]*Advanced Microscopy Program, Center for Systems Biology and Wellman Center for Photomedicine, Massachusetts General Hospital, Harvard Medical School, CPZN 8238, 185 Cambridge Street, Boston, MA 02114, USA*

[2]*Department of Biomedical Engineering, Boston University, Boston, MA 02215, USA*

*lin@helix.mgh.harvard.edu

Abstract: The bone marrow is an important site where all blood cells are formed from hematopoietic stem cells and where hematologic malignancies such as leukemia emerge. It is also a frequent site for metastasis of solid tumors such as breast cancer and prostate cancer. Intravital microscopy is a powerful tool for studying the bone marrow with single cell and sub-cellular resolution. To improve optical access to this rich biological environment, plasma-mediated laser ablation with sub-microjoule femtosecond pulses was used to thin cortical bone. By locally removing a superficial layer of bone (local laser osteotomy), significant improvements in multiphoton imaging were observed in individual bone marrow compartments *in vivo*. This work demonstrates the utility of scanning laser ablation of hard tissue with sub-microjoule pulses as a preparatory step to imaging.

OCIS codes: (120.0120) Instrumentation, measurement, and metrology; (170.1020) Ablation of tissue; (180.5810) Scanning microscopy.

References and links

1. I. Mazo, J. Gutierrez-Ramos, P. S. Frenette, R. O. Hynes, D. D. Wagner, and U. H. von Adrian, "Hematopoietic progenitor cell rolling in bone marrow microvessels: parallel contributions by endothelial selectins and vascular cell adhesion molecule 1," J. Exp. Med. **188**, 465–474 (1998).
2. C. Lo Celso, H. E. Fleming, J. W. Wu, C. X. Zhao, S. Miake-Lye, J. Fujisaki, D. Côté, D. W. Rowe, C. P. Lin, and D. T. Scadden, "Live-animal tracking of individual haematopoietic stem/progenitor cells in their niche." Nature **457**, 92–96 (2009).
3. A. Colmone, M. Amorim, A. L. Pontier, S. Wang, E. Jablonski, and D. A. Sipkins, "Leukemic Cells Create Bone Marrow Niches That Disrupt the Behavior of Normal Hematopoietic Progenitor Cells," Science **322**, 1861–1865 (2008).
4. C. Lo Celso, J. W. Wu, and C. P. Lin, "In vivo imaging of hematopoietic stem cells and their microenvironment." J. Biophotonics **2**, 619–631 (2009).
5. M. Firbank, M. Hiraoka, M. Essenpreis, and D. T. Delpy, "Measurement of the optical properties of the skull in the wavelength range 650-950 nm." Phys. Med. Biol. **38**, 503–510 (1993).
6. H.-T. Xu, F. Pan, G. Yang, and W.-B. Gan, "Choice of cranial window type for in vivo imaging affects dendritic spine turnover in the cortex." Nat. Neurosci. **10**, 549–551 (2007).
7. A. Amendola and D. E. Bonasia, "Results of high tibial osteotomy: review of the literature." Int. Orthop. **34**, 155–160 (2010).
8. B. J. Schaller, R. Gruber, H. A. Merten, T. Kruschat, H. Schliephake, M. Buchfelder, and H. C. Ludwig, "Piezoelectric Bone Surgery: A Revolutionary Technique for Minimally Invasive Surgery in Cranial Base and Spinal Surgery? Technical Note," Neurosurgery **57**, E410 (2005).

#217646 - $15.00 USD Received 23 Jul 2014; revised 15 Aug 2014; accepted 17 Aug 2014; published 12 Sep 2014

9. A. Holtmaat, T. Bonhoeffer, D. K. Chow, J. Chuckowree, V. De Paola, S. B. Hofer, M. Hübener, T. Keck, G. Knott, W.-C. A. Lee, R. Mostany, T. D. Mrsic-Flogel, E. Nedivi, C. Portera-Cailliau, K. Svoboda, J. T. Trachtenberg, and L. Wilbrecht, "Long-term, high-resolution imaging in the mouse neocortex through a chronic cranial window." Nat. Protoc. **4**, 1128–1144 (2009).
10. R. D. Piper, G. A. Lambert, and J. W. Duckworth, "Cortical blood flow changes during spreading depression in cats." Am. J. Physiol. **261**, H96–H102 (1991).
11. A. Arieli, A. Grinvald, and H. Slovin, "Dural substitute for long-term imaging of cortical activity in behaving monkeys and its clinical implications." J. Neurosci. Methods **114**, 119–133 (2002).
12. D. C. Jeong, P. S. Tsai, and D. Kleinfeld, "Prospect for feedback guided surgery with ultra-short pulsed laser light." Curr. Opin.Neurobiol. **22**, 1–10 (2011).
13. D. C. Jeong, P. S. Tsai, and D. Kleinfeld, "All-optical osteotomy to create windows for transcranial imaging in mice," Opt. Express **21**, 23160–23168 (2013).
14. A. Vogel and V. Venugopalan, "Mechanisms of pulsed laser ablation of biological tissues." Chem .Rev. **103**, 577–644 (2003).
15. L. T. Cangueiro, R. Vilar, A. M. Botelho do Rego, and V. S. F. Muralha, "Femtosecond laser ablation of bovine cortical bone." J. Biomed. Opt. **17**, 125005 (2012).
16. P. S. Tsai, P. Blinder, B. J. Migliori, J. Neev, Y. Jin, J. A. Squier, and D. Kleinfeld, "Plasma-mediated ablation: an optical tool for submicrometer surgery on neuronal and vascular systems." Curr. Opin. Biotechnol. **20**, 90–99 (2009).
17. P. S. Tsai, B. Friedman, A. I. Ifarraguerri, B. D. Thompson, V. Lev-ram, C. B. Schaffer, Q. Xiong, R. Y. Tsien, J. A. Squier, and D. Kleinfeld, "All-Optical Histology Using Ultrashort Laser Pulses Neurotechnique," Neuron **39**, 27–41 (2003).
18. H. U. Fried, H. D. Linnig, and S. I. Korsching, "An inexpensive mouse headholder suitable for optical recordings." Physiol. Behav. **74**, 253–255 (2001).
19. I. Veilleux, J. A. Spencer, D. P. Biss, D. Côté, and C. P. Lin, "In Vivo Cell TrackingWith Video Rate Multimodality Laser Scanning Microscopy," IEEE J. Sel. Top. Quant. **14**, 10–18 (2008).
20. C. Lo Celso, C. P. Lin, and D. T. Scadden, "In vivo imaging of transplanted hematopoietic stem and progenitor cells in mouse calvarium bone marrow," Nat. Protoc. **6**, 1–14 (2011).
21. J. Schindelin, I. Arganda-Carreras, E. Frise, V. Kaynig, M. Longair, T. Pietzsch, S. Preibisch, C. Rueden, S. Saalfeld, B. Schmid, J.-Y. Tinevez, D. J. White, V. Hartenstein, K. Eliceiri, P. Tomancak, and A. Cardona, "Fiji: an open-source platform for biological-image analysis." Nat. Methods **9**, 676–682 (2012).
22. Y. Liu and M. Niemz, "Ablation of femural bone with femtosecond laser pulses–a feasibility study." Las. Med. Sci **22**, 171–174 (2007).
23. W. B. Armstrong, J. A. Neev, L. B. D. Silva, A. M. Rubenchik, and B. C. Stuart, "Ultrashort Pulse Laser Ossicular Ablation and Stapedotomy in Cadaveric Bone," Laser Surg. Med. **30**, 216–220 (2002).
24. D. N. Vitek, D. E. Adams, A. Johnson, P. S. Tsai, S. Backus, C. G. Durfee, D. Kleinfeld, and J. A. Squier, "Temporally focused femtosecond laser pulses for low numerical aperture micromachining through optically transparent materials." Opt. Express **18**, 18086–18094 (2010).
25. L. Cangueiro and R. Vilar, "Influence of the pulse frequency and water cooling on the femtosecond laser ablation of bovine cortical bone," App. Surf. Sci. **283**, 1012–1017 (2013).
26. C. Tulea, J. Caron, H. Wahab, N. Gehlich, M. Hoefer, D. Esser, B. Jungbluth, A. Lenenbach, and R. Noll, "Highly efficient nonthermal ablation of bone under bulk water with a frequency-doubled Nd:YVO 4 picosecond laser," SPIE Proc. Ser. **8565**, 85656E (2013).
27. V. G. Pursel, R. J. Wall, C. E. J. Rexroad, R. E. Hammer, and R. L. Brinster, "A rapid whole-mount staining procedure for nuclei of mammalian embryos," Theriogenology **24**, 687–691 (1985).
28. R. Savic, L. Luo, A. Eisenberg, and D. Maysinger, "Micellar Nanocontainers Distribute to Defined Cytoplasmic Organelles," Science **300**, 615–618 (2003).
29. E. Hecht, *Optics* (Pearson Education Inc, Paris, 2002), 4th ed.
30. M. Zhang, S. Xuan, M. L. Bouxsein, D. von Stechow, N. Akeno, M. C. Faugere, H. Malluche, G. Zhao, C. J. Rosen, A. Efstratiadis, and T. L. Clemens, "Osteoblast-specific knockout of the insulin-like growth factor (IGF) receptor gene reveals an essential role of IGF signaling in bone matrix mineralization." J. Biol. Chem. **277**, 44005–44012 (2002).
31. J. A. Spencer, F. Ferraro, E. Roussakis, A. Klein, J. Wu, J. M. Runnels, W. Zaher, L. J. Mortensen, C. Alt, R. Turcotte, R. Yusuf, D. Côté, S. A. Vinogradov, D. T. Scadden, and C. P. Lin, "Direct measurement of local oxygen concentration in the bone marrow of live animals." Nature **508**, 269–273 (2014).
32. A. K. Dunn, V. P. Wallace, M. Coleno, M. W. Berns, and B. J. Tromberg, "Influence of optical properties on two-photon fluorescence imaging in turbid samples," Appl. Optics **39**, 1194–1201 (200).
33. M. S. Starosta and A. K. Dunn, "Three-dimensional computation of focused beam propagation through multiple biological cells," Opt. Express **17**, 898–905 (2009).
34. B. Girard, D. Yu, M. R. Armstrong, B. C. Wilson, C. M. L. Clokie, R. Dwayne Miller, and R. J. D. Miller, "Effects of femtosecond laser irradiation on osseous tissues," Laser Surg. Med. **39**, 273–285 (2007).
35. M. Cloutier, B. Girard, S. A. F. Peel, D. Wilson, G. K. B. Sándor, C. M. L. Clokie, and D. Miller, "Calvarial

#217646 - $15.00 USD Received 23 Jul 2014; revised 15 Aug 2014; accepted 17 Aug 2014; published 12 Sep 2014

bone wound healing: a comparison between carbide and diamond drills, Er:YAG and Femtosecond lasers with or without BMP-7." Oral Surg. Oral Med. O. **110**, 720–728 (2010).
36. G. Nicolodelli, R. D. F. Z. Lizarelli, and V. S. Bagnato, "Influence of effective number of pulses on the morphological structure of teeth and bovine femur after femtosecond laser ablation." J. Biomed. Opt. **17**, 048001 (2012).
37. Y. C. Lim, K. J. Altman, D. F. Farson, and K. M. Flores, "Micropillar fabrication on bovine cortical bone by direct-write femtosecond laser ablation." J. Biomed. Opt. **14**, 064021 (2009).
38. R. An, G. W. Khadar, E. I. Wilk, B. Emigh, H. K. Haugen, G. R. Wohl, B. Dunlop, M. Anvari, J. E. Hayward, and Q. Fang, "Ultrafast laser ablation and machining large-size structures on porcine bone." J. Biomed. Opt. **18**, 70504 (2013).
39. P. A. Quinto-Su and V. Venugopalan, "Mechanisms of laser cellular microsurgery." in "Laser manipulation of cells and tissues," , vol. 82, M. Berns and K. O. Greulich, eds. (Elsevier - Methods in cell biology, Amsterdam, 2007), chap. 4, pp. 113–151.
40. D. D. Lo, Mackanos, M. A. Chung, M. T. Hyun, J. S, D. T. Montoro, M. Grova, C. Liu, J. Wang, D. Palanker, A. J. Connolly, M. T. Longaker, C. H. Contag, and D. C. Wan, "Femtosecond Plasma Mediated Laser Ablation Has Advantages Over Mechanical Osteotomy of Cranial Bone," Laser Surg. Med. **44**, 805–814 (2012).
41. M. Yildirim, O. Ferhanoglu, J. Kobler, S. M. Zeitels, and A. Ben-Yakar, "Parameters affecting ultrafast laser microsurgery of subepithelial voids for scar treatment in vocal folds," J. Biomed. Opt. **18**, 118001 (2013).
42. A. L. Carlson, J. Fujisaki, J. Wu, J. M. Runnels, R. Turcotte, C. L. Celso, D. T. Scadden, T. B. Strom, and C. P. Lin, "Tracking single cells in live animals using a photoconvertible near-infrared cell membrane label." PLOS ONE **8**, e69257 (2013).

1. Introduction

The concept of stem cell niches, where stem cells reside, implies that the position of cells in biological tissue regulates their function. Confocal and multiphoton scanning microscopy are commonly used to describe the microenvironment of hematopoietic stem/progenitor cells (H-SPC) and cancer cells in the bone marrow (BM) [1–3]. Live animal imaging of the BM is usually performed in the skull calvarial bone through a relatively thin (50-75 μm) hard bone matrix [4]. However, imaging through highly scattering bone yields image quality that is not maximal and limited imaging depth [5]. Therefore, approaches are needed to maintain the diffraction limited focus, and hence improve the optical signal generation and detection.

A straightforward approach, osteotomy, consists of thinning the bone. Osteotomy has been performed for decades with mechanical tools and found many applications [6,7]. In particular, cranial osteotomy has served as a means to increase access to the central nervous system by removing most of the overlying bone, including the BM space [8,9]. Although multiple protective layers of the central nervous system separate bone from the brain (dura mater, arachnoid membrane and pia mater), mechanical osteotomy can have deleterious effects on the brain [6,10,11]. For imaging the BM, which is located 50-75 μm below the bone surface in the skull, the precision required to remove less than 50 μm of hard cortical and spare the BM from damage by far exceeds the capability of mechanical tools.

Recently, plasma-mediated laser ablation has been proposed as a non-mechanical alternative for *in vivo* cranial osteotomy [12]. The method was combined with second-harmonic generation (SHG) metrology for complete automation. More importantly, the brain tissue viability was preserved as assessed by histology and functional imaging [13]. The advantage of femtosecond plasma-mediated laser ablation resides in the decreased energy imparted on the tissue. The fluence threshold for ablation decreases by 3 orders of magnitude as the pulse duration is reduced from nanosecond to femtosecond [14]. It is therefore possible to remove a small volume of tissue per laser pulse ($\sim$1 μm^3), while minimizing thermomechanical damage [14]. Characterization of the ablation threshold in bone has been performed under different conditions and is usually found to be $\sim$1 J/cm^2 [15], or 10 nJ for a 1 μm^2 focal spot [16].

#217646 - $15.00 USD Received 23 Jul 2014; revised 15 Aug 2014; accepted 17 Aug 2014; published 12 Sep 2014

Practical implementations of all-optical cranial osteotomy and histology of the brain usually employ higher pulse energies as the speed of tissue removal is also an important parameter (e.g. 8 μJ and 10 μm axial step) [13,17]. Performing osteotomy for BM imaging requires more precision as only a thin layer of cortical bone needs to be removed and the site to be imaged is immediately adjacent to the surgery site, i.e. no protective layers are present. In this work, we sequentially remove thin layers (2 μm) of cortical bone to expose a single BM compartment using a pulse energy (0.3 μJ) closer to the ablation threshold, where the most significant advantages of femtosecond laser ablation (high spatial precision and spatially-confined collateral damages) is realized. Our primary goal is to characterize the improvements in two-photon excited fluorescence (TPEF) signal from cells residing in the BM.

2. Materials and methods

2.1. Animals

All animal experiments were performed in compliance with institutional guidelines and approved by the Subcommittee on Research Animal Care (SRAC) at Massachusetts General Hospital. Actin-GFP knock-in mice (C57BL/6-Tg(CAG-EGFP) 131Osb/LeySopJ) and C57BL/6 mice were purchased from the Jackson Laboratory (Bar Harbor, ME). Col2.3-GFP knock-in mice were kindly provided by Prof. David Scadden. To image the skull and perform optical osteotomy, mice were anesthetized with isoflurane gas, and placed in an heated holder. A bite bar and a set of 4 head screws held the head steady during microsurgery to minimize motion artifacts [18]. The skull was exposed by making an incision in the scalp.

2.2. Scanning optical microscopy

A titanium:sapphire laser (80 MHz, Mai Tai HP, Spectra Physics) was scanned at 30 frame per second by spinning polygon (model BMC7, Lincoln Laser) and galvanometer (model 6240H, Cambridge Technology) mirrors (Fig. 1(a)) [19]. Multiphoton excitation power at 860 nm can be adjusted using a half-wave plate (WPH05M-633, Thorlabs). Second-harmonic generation (SHG) from cortical bone collagen was collected at 420nm (FF01-417/60-25, Semrock) and two-photon excited fluorescence (TPEF) from GFP at 525 nm (FF01-525/45-25, Semrock). A 808 nm notch filter (NF03-808E-25, Semrock) and a 650 nm short-pass filter (FF01-650/SP-25) eliminated the laser light and dichroics separate multiphoton emission light (720dcxru Chroma and FF458-Di02-25-36 Semrock). The multiphoton emission light was detected by large area photomultiplier tubes (PMT, R7600U series, Hamamatsu).

Measurements were made on the skull between the sagittal suture bifurcation and the intersection of sagittal and coronal sutures. More detailed information about the location of bone marrow comportments in mouse skulls can be found in Lo Celso *et al.* 2009 and 2011 [2,20]. B-M images are always captured transversally, but three-dimensional reconstructions can be made to show sagittal or coronal sections. All images at a same location were recorded with the same excitation and detection parameters. Image post-processing and analysis was performed using Fiji and Matlab. Fiji is an open-source image processing package largely based on ImageJ that focuses on biological image analysis [21].

#217646 - $15.00 USD Received 23 Jul 2014; revised 15 Aug 2014; accepted 17 Aug 2014; published 12 Sep 2014

2.3. *Femtosecond laser bone thinning*

Plasma-mediated laser ablation was performed using femtosecond pulses from a regenerative amplifier (380 fs, 10.5 kHz repetition rate, RegA 9000, Coherent). The regenerative amplifier was seeded by the Mai Tai beam and pumped by 10 W of a CW laser (532 nm, Verdi, Coherent). Volumetric ablation was achieved by scanning the beam laterally with a 2D galvanometer mirrors set (GVSM002, Thorlabs) and moving the sample axially with an automated 3D translational stage (Sutter ROE-200, MPC-385, Research Precision Instrument). The 2D-scanning unit was synchronized by the image acquisition software via a hardware control card (NI USB-6211, National Instruments) for the slow axis and a function generator (AFG320, Tektronix) for the fast axis (Fig. 1(a)). The fast axis moved at 15 mm/s at the sample plane. Adjacent pulses of 0.3 μJ were displaced by 1.45 μm. A flushing system was integrated onto the objective to continuously remove debris and ensure uninterrupted surgery. (Fig. 1(b)).

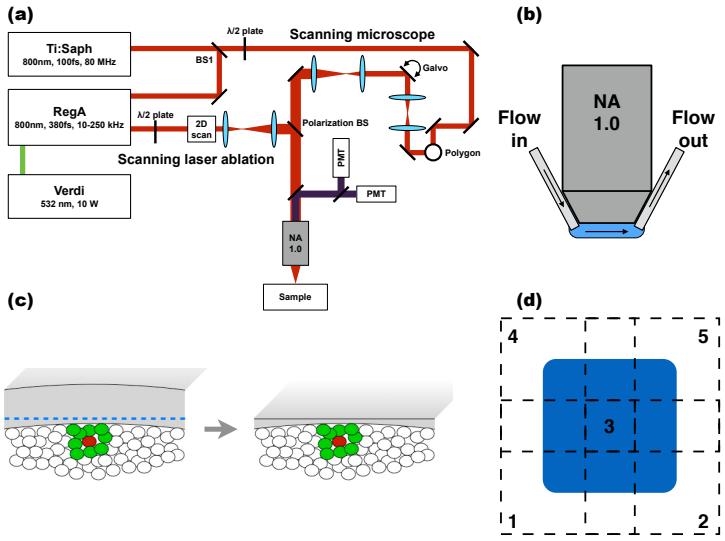

Fig. 1. Laser osteotomy system and method. (a) Schematic of the optical platform. (b) In order to flush debris from the ablation site, the immersion solution (Normal saline, Sigma-Aldrich) was circulated at high flux through a pair of needles (Gauge 26, 1.3 cm length, Fisher Scientific) affixed onto the objective lens (60X, 1.0 NA, LUMPLFLN, Olympus) and connected to a peristaltic pump (Ismatec, Harvard Apparatus). (c) To improve optical access to HSPC (red) and their neighboring cells (green), cortical bone over one specific BM compartment is removed and only a thin layer of bone is left. (d) Five overlapping areas were ablated sequentially (region 1 to 5) to provide a full field-of-view (region 3) where optical access is improved.

Using the system described above, we aimed to perform local laser osteotomy, where the cortical bone overlying a single BM compartment is thinned. Specific compartments can be selected depending on their cellular content (Fig. 1(c)). To generate a full field-of-view with improved optical access, five overlapping areas were ablated (Fig. 1(d)). The beam is scanned once per axial plane. After single-pass ablation, the sample was moved up by 2 μm until 10 μm of cortical bone were removed at one location. The animal was then moved by 125 μm to an adjacent area. These two steps were repeated until 10 μm of cortical bone was removed at all five locations. This process was repeated 4 time such that a total thickness of 40 μm of bone is removed. This iterative process is completely automated and can be completed in a single sequence. All laser ablation performed in this work was done on live mice.

#217646 - $15.00 USD Received 23 Jul 2014; revised 15 Aug 2014; accepted 17 Aug 2014; published 12 Sep 2014

3. Results

3.1. Characterization of local laser osteotomy

Local laser osteotomy was successfully performed with 0.3 μJ pulses (10 J/cm^2 fluence). The 0.3 μJ pulse energy was determined empirically by its ability to perform single-pass scanning laser ablation for a fixed pulse separation and axial step size. The line scanning frequency was first fixed to 20 Hz such that adjacent pulses would overlap (1.45 μm center-to-center). The axial step between ablation planes, corresponding to the ablation depth, has a major impact on the ablation speed. In order to maximize the speed, the axial step was set to 2 μm. This allows for completion of the process in less than 20 minutes.

Although the total microsurgery time is suitable for live animal studies, the ablation speed of 3x10^{-5} mm^3/s is smaller than previously reported values varying between 0.02 and 0.15 mm^3/sec [17, 22]. This is to be expected when more than 10 times lower pulse energy is used at a similar repetition rate. The efficiency of 9.17 μm^3/μJ was found to be similar to previous studies [23–25]. The ablation efficiency critically depends on the rate of debris removal. The flushing system is therefore an indispensable component [26].

3.2. Characterization of TPEF imaging after osteotomy

The improvement in optical access to the BM after local laser osteotomy was assessed for TPE-F imaging using two different transgenic mouse models expressing GFP. First, we quantified signal intensity and contrast changes at the endosteum, where the cortical bone and the BM intersect, using Col2.3-GFP mice. Most osteolineage cells, an established component of the HSPC niche, are found on the endosteum. The Col2.3-GFP knock in mice in which osteolineage cells express GFP can therefore serve as a model to test whether local laser osteotomy can improve the imaging of the HSPC endosteal microenvironment. Second, changes in signal intensity and spatial frequency content throughout the BM as a function of depth were evaluated using actin-GFP mice. Actin-GFP mice have a large number of GFP-expressing cells uniformly distributed in the BM.

Bone thinning was successfully performed in Col2.3-GFP mice *in vivo* and typical images before and after ablation are shown in Fig. 2(a,b). From those images, it is clear that the TPEF signal is increased at the endosteum. The increase in signal is formally quantified at multiple locations, all in the 60-70 μm depth range prior to ablation. For each field-of-view, an axial-stack is recorded after removing 0, 20 and 40 μm of cortical bone and maximum intensity projection images are produced with Fiji [21]. The image after removal of 40 μm of cortical bone is used to generate a binary mask, again in Fiji, using the maximum entropy method. The intensity increase is then evaluated within the mask using a Matlab script. The results of the relative TPEF intensity increase are shown in Fig. 2(c). Removing only 20 μm of bone is sufficient to observe an increase (1.8x) in TPEF signal intensity, while the intensity is almost four-fold higher (3.9x) at the endosteum by removing 40 μm.

To compare spatial resolution, we first adjusted the dynamic range of images before bone thinning (Fig. 3(a)). Zooming in on a single osteolineage cell reveals that the cytoplasm and nucleus are more easily discernible, which is indicative of a good image quality for thick tissue TPEF microscopy. The latter observation is important as evaluating the number of osteolineage cells or osteolineage cell layers requires visualizing nuclei, which would otherwise require the injection of a nuclear dye. To validate the identification of nuclei using the GFP signal in the Col2.3-GFP mouse model, we co-labelled Col2.3-GFP osteolineage cells with a nuclear stain (by in vivo injection of Hoechst 33342 - 200 μL at 10 mg/mL retro-orbitally) [27, 28]. The co-registration of the Hoechst and brighter GFP signals confirms the identification of the brighter GFP area within osteolineage cells as being nuclei (data not shown). To quantify the improve-

#217646 - $15.00 USD Received 23 Jul 2014; revised 15 Aug 2014; accepted 17 Aug 2014; published 12 Sep 2014

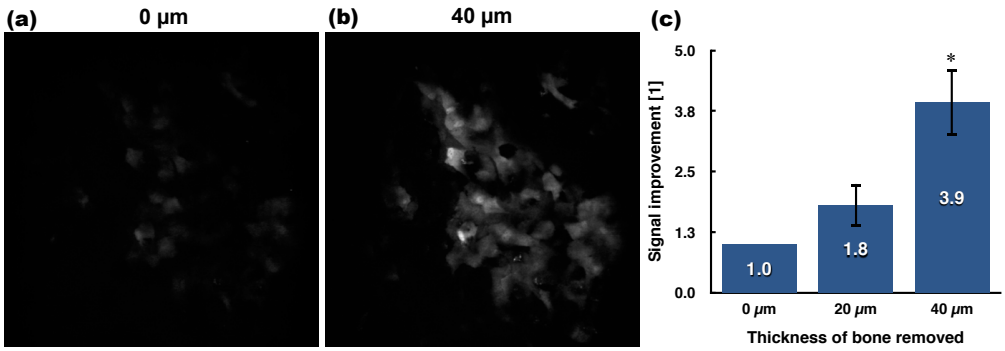

Fig. 2. TPEF signal increase at the endosteum. Maximum-intensity projection images of GFP-expressing osteolineage cells residing at the endosteum (a) before and (b) the removal of 40 μm of bone. More cells are visible after local osteotomy, illustrating the increase in TPEF signal. Image width: 360 μm. (c) Quantification of TPEF signal improvement as a function of bone removed (n=3, *one-sided paired t-test with Bonferroni correction on absolute intensity - standard deviation).

ment in lateral contrast on individual cells, the contrast between the nucleus and cytoplasm is evaluated in osteolineage cells using Eq. (1) [29]. To measure the contrast, a 10-pixel long line profile is drawn in FIJI and averaged over a width of 5 pixels. Using this method, the contrast is evaluated to increase by a factor of two after removing 20 μm and of three after 40 μm (Fig. 3(c)).

$$Contrast = \frac{I_{max} - I_{min}}{I_{max} + I_{min}}. \tag{1}$$

The spatial resolution in the axial dimension is also expected to improve. As osteolineage cells lining the endosteum are flat and thin, their axial profile through a 10x10 pixels^2 area in the cytoplasm is measured. The thickness of the osteolineage cells was measured to be 4.7$\pm$1.3 μm on average, whereas they were 1.5x thicker before bone thinning (Fig. 3(d)). In comparison, the known value obtained using standard histomorphometry methods is of 3.5 μm [30].

To investigate if TPEF imaging improvements are preserved away from the endosteum deeper into the BM, local laser osteotomy was performed in actin-GFP mice. A three-dimensional reconstruction and a single plane image 20 μm away from the endosteum are shown in Fig. 4(a,c) before and Fig. 4(b,d) after bone thinning. More excitation power could have been used to obtain stronger TPEF signal before ablation, but the GFP signal would have been largely saturated following ablation, making quantification difficult.

To quantify the improvement as a function of depth, the average TPEF signal is measured in different regions (n=5) using Fiji (Fig. 4(e)). The ratio between the two curves before and after ablation, or the intensity gain factor, indicates that the TPEF intensity increase is stronger at the endosteum. The intensity gain factor after ablation decreases with depth, but remains as large as a factor of 3 to a depth of 50 μm. By fitting an exponential to the TPEF signal decay as a function of depth, the total attenuation coefficient of the BM was found to be 35 mm^{-1} prior to osteotomy.

The spatial frequency content in the Fourier space was analyzed to characterize changes in the lateral profile of the TPEF point spread function as a function of depth. To this end, fast Fourier transform (FFT) of actin-GFP images were evaluated at every depth and the DC component was removed. The FFT was then fit at every depth to a gaussian profile. The power spectral density, which is proportional to the square of the FFT, contains the information of in-

#217646 - $15.00 USD Received 23 Jul 2014; revised 15 Aug 2014; accepted 17 Aug 2014; published 12 Sep 2014

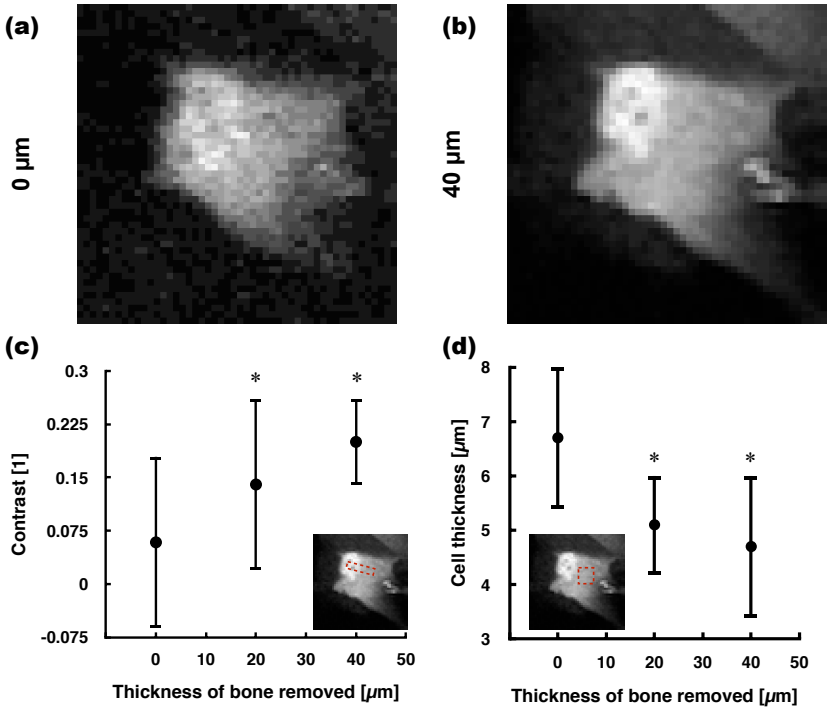

Fig. 3. Lateral contrast and axial resolution improvement at the endosteum. The images show a single osteolineage cell (a) before and (b) after laser osteotomy. The dynamic range was adjusted in order to show that more spatial details become visible. Image width: 36 μm. (c) The lateral contrast between cell nuclei and their cytoplasm was significantly larger after removing 20 and 40 μm of bone (n=16). The contrast is evaluated between two bright fluorescent structures such that the measurement is independent of intensity increase effects. (d) For the axial dimension, the thickness of osteolineage cells at the endosteum was measured (n=15). A paired Wilcoxon signed rank tests with Bonferroni correction was performed in (c) and (d) - standard deviation.

terest about the image spatial frequency content. The $1/e^2$ width of the power spectral density was defined as the lateral spatial frequency bandwidth. The lateral frequency bandwidth as a function of depth is plotted in Fig. 4(f). The vertical difference between the two curves represents the relative increase in spatial frequency content, related to an improvement in lateral profile of the TPEF point spread function. The bandwidth gain factor as a function of depth is not shown as it was relatively uniform (1.9 ± 0.3) in the depth range from 0 to 60 μm. It is important to note that the bandwidth is not a direct measure of the spatial resolution. This is because the power spectral density characterizes both the TPEF point spread function and the size of imaged objects. In BM images of actin-GFP mice, many cells are visible, but only a limited number of smaller objects are present. The bandwidth is therefore expected to be on the order of the size of a cell.

#217646 - $15.00 USD Received 23 Jul 2014; revised 15 Aug 2014; accepted 17 Aug 2014; published 12 Sep 2014

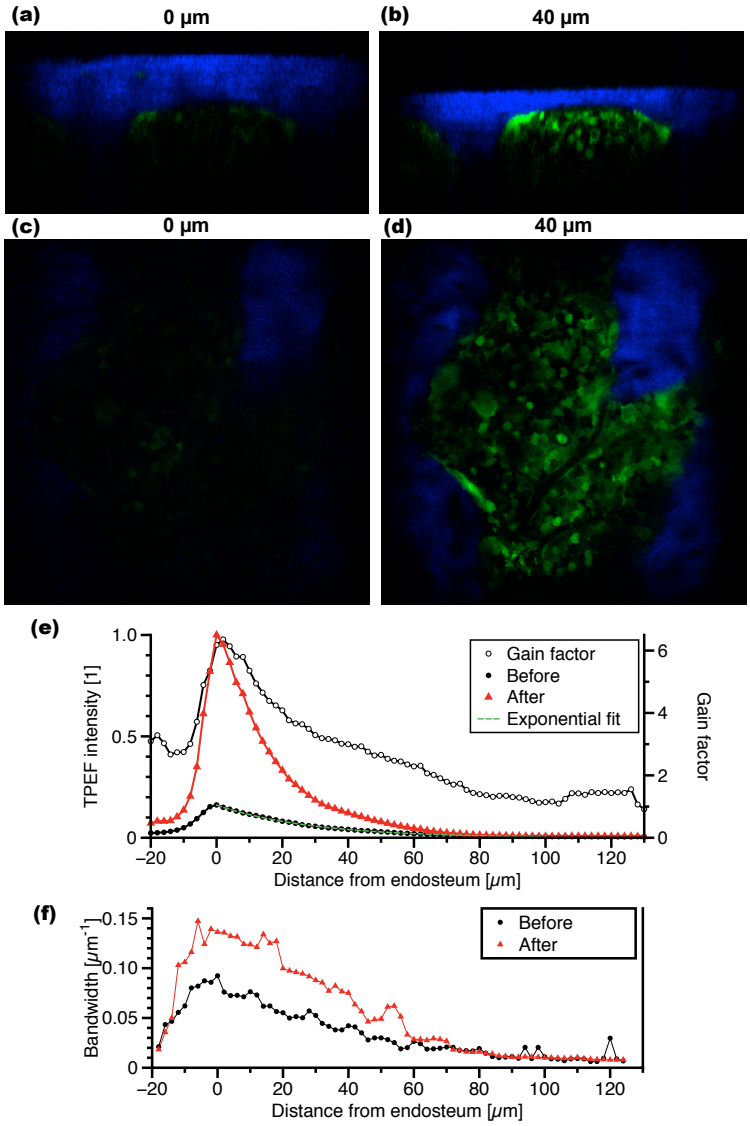

Fig. 4. Imaging improvement with depth in the BM. The top row images are three-dimensional reconstructions of sagittal cross-sections (a) before and (b) after local laser osteotomy. Cortical bone (blue) sits on top of a BM compartment containing GFP+ cells (green). The second row images show a single axial plane in the BM (c) before and (d) after local laser osteotomy. Image width: 360 μm. (e) The relative TPEF intensity from actin-GFP cells is plotted as a function of depth before and after local laser osteotomy. Flat regions at the endosteum were selected (n=5) and the cumulative GFP signal in each axial plane was normalized to the maximum cumulative intensity at the endosteum. (f) The lateral spatial frequency bandwidth is plotted as a function of depth before and after local laser osteotomy.

#217646 - $15.00 USD Received 23 Jul 2014; revised 15 Aug 2014; accepted 17 Aug 2014; published 12 Sep 2014

4. Discussion

We have obtained significant improvements in TPEF imaging of the BM following local laser osteotomy by removing superficial layers (20-40 μm) of bone. We have documented the improvement both at the endosteum (immediately below the cortical bone) and deeper into the BM using two different mouse models whose GFP+ cells are either lining the endosteal surface (Col2.3-GFP) or dispersed throughout the BM cavity (actin-GFP). Using the latter, the increase in imaging depth after osteotomy is found to be comparable to the thickness of bone removed, suggesting that the bone is not the sole scattering layer. Indeed, the attenuation coefficient of the BM is found to be very high (35 mm^{-1}) and is close to that of the bone. Such a high attenuation coefficient can be expected for the BM as it has a high cellularity and is highly vascularized [31].

Bone thinning affects the incident illumination in two ways. First, cortical bone removal decreases scattering as the bone is a highly scattering material (the scattering coefficient of bone is $\sim$30 mm^{-1} [5]). Second, the calvarial bone is curved. Flattening the bone surface minimizes aberrations due to the outer skull curvature. Both the decrease in scattering and reduction in aberrations should translate into the improvement of the TPEF point spread function (PSF). The measured changes in contrast, axial profile and lateral spatial frequency content are all consistent with improvement in the PSF. Previous studies on the effects of tissue optical properties on TPEF imaging have shown, both by simulation and experimentally, that the lateral resolution was largely unaffected by the turbidity of the sample [32, 33]. It is therefore more likely that the improvement in the PSF observed in our studies is mainly due to flattening of the skull surface and minimizing optical aberrations. Nevertheless, the total amount of bone removed is important in providing increased optical access to the BM. In future studies, it may be preferable to measure, prior to ablation, the thickness of the bone over the region of interest (using SHG). Ablation can then be performed until a constant thickness ($\sim$10 μm) of bone remains, rather than ablating a constant depth as is performed in this study.

The speed of ablation is an important consideration for in vivo studies. The length of time a mouse can be kept on stage is typically about 2 hours, so the time it takes to thin the bone should be a fraction of an hour in order to leave time for imaging experiments. Imaging speed can be increased by using higher pulse energies [15, 22, 25, 34–36] but at the expense of increasing the risk of collateral damage and compromising spatial control. A solution for the future is to implement an ablation scheme where the pulse energy is adjusted as a function of depth. A larger pulse energy, and thus a larger axial step size, can be used at the surface, while a minimal pulse energy should be used in the vicinity of the BM to minimize possible damage [37–39]. Local laser osteotomies performed in this work caused no visible changes in the structure of the BM. The technique is therefore useful for structural imaging, where imaged objects are stationary on the time scale of the experiment. For the study of dynamic processes such as cell migration, it will be important to carefully assess whether bone thinning leads to specific functional alterations of the BM. The assessment should directly relate to the biological process of interest as the sensitivity to external stressors for different processes is not known a priori.

The purpose of this work is to improve cellular imaging in the bone marrow for studying hematopoietic stem cell biology and cancer biology in mouse models. These studies require cell labeling with fluorescent proteins or probes and are therefore more suitable as research tools rather than for direct human translation. Label-free techniques have yet to be shown to be useful for bone marrow imaging. On the other hand, femtosecond laser osteotomy or laser scar removal may find clinical use in a different context, as discussed by Lo *et al.* and Yildirim *et al.* [40, 41].

#217646 - $15.00 USD Received 23 Jul 2014; revised 15 Aug 2014; accepted 17 Aug 2014; published 12 Sep 2014

5. Conclusion

We investigated the use of sub-microjoule femtosecond laser pulses to perform plasma-mediated ablation of hard cortical bone in live mice. Local laser osteotomy of the calvaria is performed by raster scanning 0.3 μJ pulses on cortical bone. Osteotomy provides a window of improved optical access to the BM, both in term of the signal intensity and the PSF spatial profile. Laser ablation has no visible effect on the bone marrow organization. Structural imaging can thus be performed following local laser osteotomy. Being able to perform osteotomy in live mice is the first step toward establishing the method for imaging dynamic processes. Future studies will further investigate this aspect by evaluating possible functional response to laser bone removal. Functional validation will be important as it will extend the application of laser bone thinning not only to functional imaging, but also to other optical techniques such as oxygen sensing [31] and photo-conversion [42].

Acknowledgments

This work was supported by the HSCI grant DP-0079-11-00 and the NIH grant EB017274. RT was supported by a FRQNT PhD Fellowship and a Wellman Center for Photomedicine Graduate Student Fellowship. The authors would also like to acknowledge funding support from PCBC (U01HL099997).

#217646 - $15.00 USD Received 23 Jul 2014; revised 15 Aug 2014; accepted 17 Aug 2014; published 12 Sep 2014